

Conventional type-II superconductivity in locally noncentrosymmetric LaRh₂As₂ single crystals

J. F. Landaeta^{1,*}, A. M. León¹, S. Zwickel², T. Lühmann¹, M. Brando¹, C. Geibel¹,
E.-O. Eljaouhari^{3,4}, H. Rosner¹, G. Zwicknagl^{1,3}, E. Hassinger^{1,2,†} and S. Khim^{1,‡}

¹Max Planck Institute for Chemical Physics of Solids, 01187 Dresden, Germany

²Technical University Munich, Physics department, 85748 Garching, Germany

³Technische Universität Braunschweig, Institut für Mathematische Physik, Mendelssohnstraße 3, 38106 Braunschweig, Germany

⁴Université de Bordeaux, CNRS, LOMA, UMR 5798, 33400 Talence, France



(Received 6 December 2021; revised 15 April 2022; accepted 19 April 2022; published 6 July 2022)

We report on the observation of superconductivity in LaRh₂As₂, which is the analog without *f* electrons of the heavy-fermion system with two superconducting phases CeRh₂As₂ [S. Khim *et al.*, *Science* **373**, 1012 (2021)]. A zero-resistivity transition, a specific-heat jump, and a drop in magnetic ac susceptibility consistently point to a superconducting transition at a temperature of $T_c = 0.28$ K. The magnetic-field temperature superconducting phase diagrams determined from field-dependent ac-susceptibility measurements reveal small upper critical fields $\mu_0 H_{c2} \approx 12$ mT for $H \parallel ab$ and $\mu_0 H_{c2} \approx 9$ mT for $H \parallel c$. The observed H_{c2} is larger than the estimated thermodynamic critical-field H_c derived from the heat-capacity data, suggesting that LaRh₂As₂ is a type-II superconductor with Ginzburg-Landau parameters $\kappa_{GL}^{ab} \approx 1.9$ and $\kappa_{GL}^c \approx 2.7$. The microscopic Eliashberg theory indicates superconductivity to be in the weak-coupling regime with an electron-phonon-coupling constant $\lambda_{e-ph} \approx 0.4$. Despite a similar T_c and the same crystal structure as the Ce compound, LaRh₂As₂ displays conventional superconductivity, corroborating the substantial role of the 4*f* electrons for the extraordinary superconducting state in CeRh₂As₂.

DOI: [10.1103/PhysRevB.106.014506](https://doi.org/10.1103/PhysRevB.106.014506)

I. INTRODUCTION

Recently, two-phase superconductivity has been reported for the heavy-fermion compound CeRh₂As₂ [1] with highly anisotropic critical fields H_{c2} and one of the highest H_{c2}/T_c values. The unique phase diagram and the large critical-field value seem to originate in the crystal structure. Unlike many unconventional “122”-superconductors which crystallize in the ThCr₂Si₂-type structure, such as the celebrated superconductors CeCu₂Si₂ [2], URu₂Si₂ [3], and doped BaFe₂As₂ [4], CeRh₂As₂ forms the CaBe₂Ge₂-type structure. In this structure, due to an exchange of Rh and As positions in half of the unit cell, inversion symmetry is broken locally at the Ce site [shown in Fig. 1(a)] while keeping an overall inversion symmetry.

As widely discussed in noncentrosymmetric superconductors, the (local or global) inversion-symmetry breaking gives rise to antisymmetric spin-orbit coupling (ASOC) [5,6]. This induces an enhancement of H_{c2} for specific field orientations for which the magnetic field is much less effective in polarizing the spins of the Cooper pairs. As a result, the Pauli limiting

becomes ineffective, allowing for higher H_{c2} . However, due to the global inversion symmetry in CeRh₂As₂, the sign of ASOC is opposite for each Ce sublayer in the unit cell, and the superconducting gap can either follow the sign change of the ASOC or not, leading to odd- and even-parity superconducting states [7–10]. This additional parity degree of freedom leads to the field-induced phase transition within the superconducting state and the enhanced H_{c2} in the high-field phase [1]. These phenomena suggest that the lack of local inversion symmetry and ASOC are key ingredients toward the two-phase superconductivity observed in CeRh₂As₂ [1]. In addition, the inherent nonsymmorphic symmetry might lead to a topological crystalline superconducting state [11,12].

The aim of this study is to characterize the La analog, LaRh₂As₂ without 4*f* electrons, reported to crystallize in the same structure but which has not been studied down to low temperatures [13]. In doing so, we are able to investigate the influence of the crystal structure itself and the role of the 4*f* electrons that are absent in the La compound. Indeed, in noncentrosymmetric heavy-fermion superconductors it was found that broken inversion symmetry is not the only requirement for unconventional superconductivity [14]. Rather, the 4*f* electrons must actually play a crucial role since all unconventional superconducting properties have not been observed in their La analogs [15,16].

We report on the single-crystal growth of LaRh₂As₂ and resistivity, specific heat and magnetic ac-susceptibility properties down to low temperatures. We observe a superconducting transition at $T_c = 0.28$ K and determine the superconducting magnetic-field H -temperature T phase diagram of H_{c2} . Estimated superconducting parameters point

*Javier.Landaeta@cpfs.mpg.de.

†Elena.Hassinger@cpfs.mpg.de.

‡Seunghyun.Khim@cpfs.mpg.de.

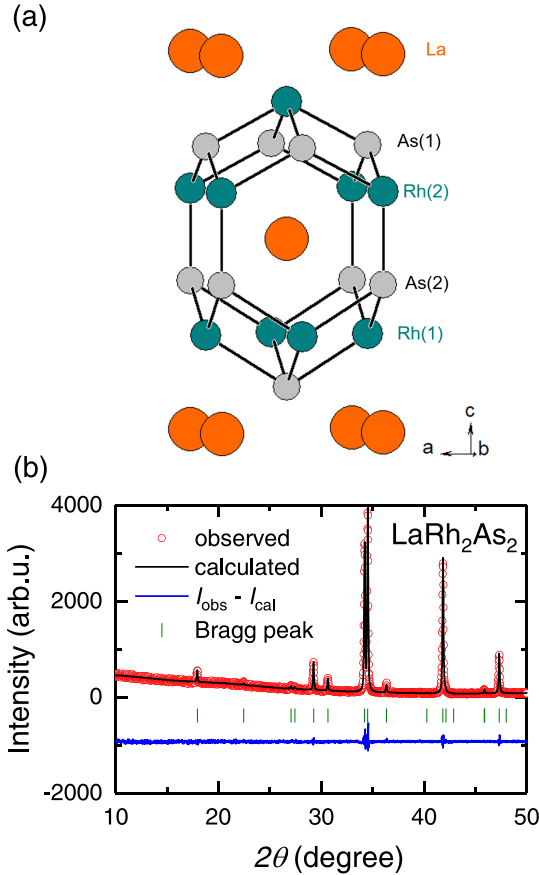


FIG. 1. (a) Crystal structure of LaRh_2As_2 (b) Powder x-ray diffraction pattern and Rietveld refinement results.

to type-II superconductivity. An estimation of the electron-phonon coupling based on the Eliashberg theory indicates weak-coupling superconductivity. Comparing the Sommerfeld coefficient deduced from a first-principles band structure calculation and the experimental value confirms the weak electron-phonon coupling. We find that—despite a similar T_c and the same crystal structure— LaRh_2As_2 displays conventional superconductivity, establishing the substantial role of the Ce-4*f* electrons for unconventional superconductivity in CeRh_2As_2 .

II. METHODS

A. Experimental methods

Single crystals of LaRh_2As_2 were grown by the Bi-flux method. Pure elements in the ratio La:Rh:As:Bi = 1:2:2:30 were placed in an alumina crucible and subsequently sealed in a quartz tube filled with 300 mbar argon. The crucible was heated to 1150 °C for 4 days and slowly cooled down to 700 °C for a week by slowly lowering the crucible in a vertical furnace. Grown single crystals were extracted by etching the Bi flux in diluted nitric acid solution. The crystal structure was analyzed by powder x-ray diffraction measurements.

The heat-capacity measurements were carried out down to 0.5 K using the relaxation-time method in a Quantum Design Physical Property Measurements System. A customized com-

pensated heat-pulse calorimeter was used between 0.04 and 4 K in a dilution refrigerator [17]. For the low-temperature measurements, the nuclear contribution was removed with the same procedure as described in Ref. [1]. At low temperatures, the contributions to the heat capacity are given by $C = C_n + C_{el} + C_{ph} = \frac{\alpha}{T^2} + \gamma_0 T + \beta T^3$ where $C_{el} + C_{ph}$ are the electronic and phonon contributions and α is the proportionality factor in the nuclear Schottky specific-heat C_n . In the case of LaRh_2As_2 as well CeRh_2As_2 , the nuclear contribution only comes from As atoms at the two crystallographic sites. From NQR measurements [18], we know that the quadrupolar splittings Δ/h for As(1) and As(2) are 31.1 and 10.75 MHz, respectively, where the nuclear spin of the As atom is $I = 3/2$ with 100% abundance. With the expression of the high-temperature term of the Schottky molar heat capacity at zero magnetic-field $\alpha = \frac{R}{4} \left(\frac{\Delta}{k_B}\right)^2$ [19], where R is the gas constant, we obtain the values of the α parameter for each As site, where the total contribution is $\alpha = 5.196 \times 10^{-6}$ JK/mol. For temperatures below 1 K, the phonon contribution is very small and can be neglected. Hence, we use $C/T = \alpha/T^3 + \gamma_0$ to remove the nuclear contribution, where $\gamma_0 = 10.5$ mJ/mol K².

The magnetic ac susceptibility was measured using a homemade set of compensated pickup coils of 2 mm length and 6000 turns each. The inner and outer diameter were 1.8 and 5 mm, respectively. A superconducting modulation coil produced the excitation field of 40 μT at 1127 Hz. The output signal of the pickup coils was amplified using a low-noise amplifier SR560 from Stanford Research Systems.

Our setup uses a National Instruments 24 bits PXIe-4463 signal generator and 24 bits PXIe-4492 oscilloscope as a data acquisition system with digital lock-in amplification. The ac-susceptibility measurements were performed for an applied field parallel and perpendicular to the tetragonal c axis using a small single crystal of a volume of $\sim 750 \mu\text{m}^3$ down to 35 mK in a MX400 Oxford dilution refrigerator. For the magnetic-field dependence of the ac-susceptibility measurements, the remnant field of the superconducting magnet was corrected. It was about ± 2 mT when sweeping the field between -25 and 25 mT as done here. It is important to remark that we started the measurement with a demagnetized magnet.

For the resistivity measurements, a standard four-point method was employed with current and voltage contacts along a line perpendicular to the c axis using an excitation current of 1 nA. The four contacts were made using 25- μm -diameter gold wires on a sample with silver paste (DuPont 4922N). The signal was amplified by a low-temperature transformer with a winding ratio of 1:100 and the output of the transformer was measured using a PXI lock-in setup at 113 Hz.

B. Computational details

Electronic-structure calculations were performed applying density-functional theory (DFT) [20,21] as implemented in the Vienna *ab initio* simulation package (VASP) [22] and the full-potential local-orbital code FPLO [23]. Both the local density approximation (LDA; in the parametrization of Perdew and Wang [24]) and the generalized

gradient approximation (GGA; in the parametrization of Perdew-Burke-Ernzerhof [25]) were used.

In the Vienna calculations a Monkhorst Pack grid of $(26 \times 26 \times 16)$ was employed; the valences of the atoms are La: $5s^2 5p^6 5d 6s^2$, Rh: $5s 4d^8$, and As: $4s^2 4p^3$. The structural optimization was performed within a force convergence of at least 10^{-3} eV/Å for each atom and a plane-wave energy cutoff of 500 eV in order to relax the internal positions and the lattice parameters. Phonon spectra were obtained by using the PHONOPY [26] program with the interatomic force constants which were calculated by VASP using the linear-response method based on density-functional perturbation theory. The calculations were performed using a supercell with 80 atoms ($2 \times 2 \times 2$ unit cell) for which the total energy were converged using a $8 \times 8 \times 6$ k -mesh and a 500 eV plane-wave cutoff.

In the FPLO calculations, the standard basis set and a $24 \times 24 \times 24$ k -mesh were applied. The spin-orbit coupling (SOC) was taken into account nonperturbatively, solving the four-component Kohn-Sham-Dirac equation.

The lattice parameters were taken from the experiment (see below). Relaxation of the internal positions was performed minimizing the total energy applying GGA. The results were robust comparing both codes and both functionals employed. For a given structure, the respective electronic structures did not show significant differences.

III. RESULTS AND DISCUSSION

A. Crystal structure

Figure 1(b) shows the powder x-ray-diffraction pattern and Rietveld-refinement results with the tetragonal CaBe_2Ge_2 -type structure [Fig. 1(a)]. We found no evidence for an additional phase nor for the ThCr_2Si_2 -type structure. The accuracy of the spectrum limits the possible amount of interchange of As and Rh to a few percentages. The determined lattice parameters $a = 4.313$ Å and $c = 9.879$ Å are comparable to the previous report [13]. Internal atomic positions were obtained by density-functional calculations (see subsection ‘‘Electronic structure calculations’’) and agree well with the closely related LaIr_2As_2 compound [27]. Compared with CeRh_2As_2 ($a = 4.280$ Å and $c = 9.861$ Å), a and c are 0.8 and 0.2% larger, respectively, explained by the absence of the Ce-4 f electron.

The structure has some similarity with the ThCr_2Si_2 -type structure, since in half of the unit cell, the Rh(1) and As(2) in the CaBe_2Ge_2 -type structure have the same layer order as the Rh and As in the centrosymmetric ThCr_2Si_2 -type structure. However, the other Rh-As layer has a completely inverted arrangement so that the As(1) atom is now at the center of the layer. Remarkably, the bond distance As(1)-Rh(2) of 2.45 Å in the ‘‘inverted’’ layer is significantly shorter than the Rh(1)-As(2) distance of 2.54 Å in the ‘‘normal’’ layer. Furthermore, the distance between the Rh(2) and the As(2) atoms with 2.41 Å is the shortest Rh-As bond in the structure, small enough to form an additional strong bond. The bonding character between these Rh(2) and As(2) atoms is evidenced in the sister compound LaNi_2As_2 , which crystallizes in both 122-polymorphs; the c -lattice parameter in the

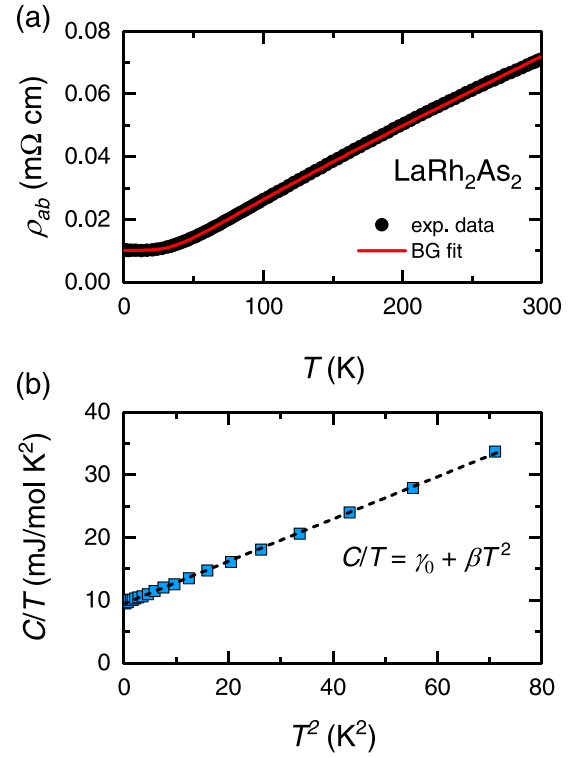


FIG. 2. (a) Temperature-dependent resistivity (circles) and the Bloch-Grüneisen fit (line). (b) Plot of C/T as a function of T^2 . The dotted line denotes the fit to the linear function $C/T = \gamma_0 + \beta T^2$, where γ_0 is the Sommerfeld coefficient and the β is the phononic specific-heat coefficient.

CaBe_2Ge_2 -type structure is substantially shorter (9.47 Å) than that in the ThCr_2Si_2 -type structure (9.93 Å) where this strong bond is absent [28].

B. Normal-state properties

The high-temperature resistivity $\rho(T)$ is shown in Fig. 2(a). The room-temperature resistivity is $\rho_{300\text{K}} = 0.079$ mΩ cm and $\rho(T)$ monotonically decreases with lowering temperatures. Due to the absence of a magnetic element in LaRh_2As_2 , the temperature dependence of $\rho(T)$ is likely attributed to electron-phonon scattering at high temperatures. Accordingly, the Bloch-Grüneisen formula is applied to fit the $\rho(T)$ data, which are written as

$$\begin{aligned} \rho(T) &= \rho_0 + \rho_{BG}(T) \\ &= \rho_0 + C_{BG} \left(\frac{T}{\Theta_R} \right)^5 \int_0^{\Theta_R/T} \frac{x^5}{(e^x - 1)(1 - e^{-x})} dx, \quad (1) \end{aligned}$$

where ρ_0 is the residual resistivity originating from imperfections of a crystalline lattice, and Θ_R is the characteristic temperature compatible with the Debye temperature. The fitted curve reproduces the experimental data up to 300 K [Fig. 2(a)] with $\Theta_R = 230$ K, $C_{BG} = 0.019$ mΩ cm, and $\rho_0 = 0.010$ mΩ cm. The residual resistivity ratio ($\text{RRR} = \rho_{300\text{K}}/\rho_0$) is about 7.

The temperature dependence of the specific heat is shown in Fig. 2(b), which follows the relation $C/T = \gamma_0 + \beta T^2$ up to ≈ 9 K, where γ_0 is the Sommerfeld coefficient and β is

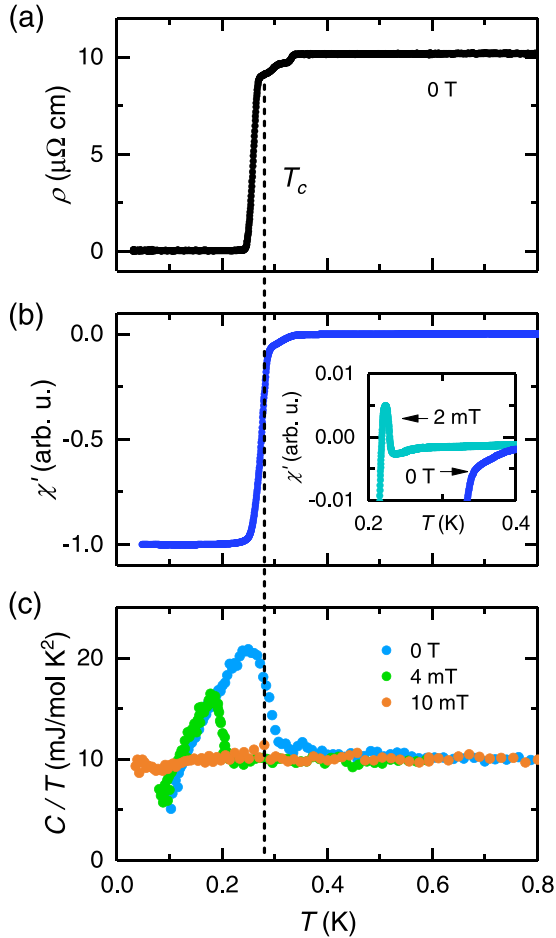


FIG. 3. (a) Temperature dependence of the resistivity $\rho(T)$ at zero field. (b) Temperature dependence of real-part of ac-susceptibility $\chi'(T)$ at zero field. The inset presents additional 2 mT data obtained for the field perpendicular to the c axis. (c) Temperature dependence of specific-heat $C/T(T)$ measured at zero, 4, and 10 mT along the c axis. The vertical dotted line denotes the superconducting transition temperature determined using the equal-entropy criterion, $T_c = 0.28$ K.

the phononic specific-heat coefficient; γ_0 is 9.4 mJ/mol K² and β is 0.34 mJ/mol K⁴. The Debye temperature given by β based on the relation $\theta_D = (12\pi^4 RN/5\beta)^{1/3}$ is 300 K, where $N = 5$ is the number of atoms in the primitive unit cell. This is larger than Θ_R determined from the Bloch-Grüneisen fit of the resistivity data. This difference is not surprising: The low-temperature specific heat probes the phonon density at very low energies, which is only determined by the velocity of the low- Q acoustic modes, which scales with the inverse mass of all elements forming the compound. Instead the increment in $\rho(T)$ at higher temperature is sensitive not only to the acoustic modes but also to the optical modes, especially the lower ones whose energy scales with the inverse mass of the heaviest element.

C. Superconducting phase transition

Figure 3 highlights the experimental evidence for the superconducting phase transition. A clear resistivity drop

appears below $T_c = 0.28$ K [Fig. 3(a)]. At the same temperature, a drop in the real part of the ac-susceptibility χ' indicates the onset of diamagnetic shielding [Fig. 3(b)]. Finally, the clear jump in C/T [Fig. 3(c)] evidences the bulk nature of the transition. An external field of 10 mT along the c axis completely suppresses the C/T anomaly, indicating that H_{c2} is of the order ~ 10 mT. The ratio $\Delta C/\gamma_0 T_c = 1.15$ is slightly smaller than the expected BCS value. This might be due to multiband superconductivity, or some fraction of the sample being nonsuperconducting, or to some additional contribution in the normal-state-specific heat. A small drop in $\rho(T)$ occurs well before the bulk T_c , likely due to spurious superconductivity caused by the presence of crystal imperfections.

D. Superconducting phase diagram

Figures 4(a) and 4(b) show the field-dependent χ' under two different field directions. The superconducting state is mainly characterized by a diamagnetic signal ($\chi' = dM/dH < 0$) below the critical field and below T_c . The onset field of the transition decreases monotonically with increasing temperatures, consistent with the nature of superconductivity. The onset field at a given temperature is higher for $H \parallel ab$ than for $H \parallel c$.

In addition, we found a small positive peak at the transition for temperatures below 200 mK as shown in the bottom panels of Figs. 4(a) and 4(b). There is a tiny peak in χ' at 250 mK as well but it does not extend to positive values. Usually such a positive peak in χ' is regarded to be the differential paramagnetic effect (DPE) that is occasionally observed in some type-I superconductors. It is attributed to the magnetization curve as a function of increasing field in which the Meissner state abruptly disappears at a critical field [29–31]. The typical behavior of the DPE is demonstrated in the field-dependent χ' of aluminum ($T_c = 1.2$ K) as shown in Fig. 4(c). In aluminum, the size of the DPE peak is comparable to the diamagnetic signal. Importantly, the DPE peak appears only at the transition from the superconducting to the normal state, on the positive (negative) field upon the up (down) sweep showing a clear irreversible character. In contrast, the χ' peak in LaRh₂As₂ is much smaller, accounting for 2% of the diamagnetic signal and it occurs reversibly in both the up and the down sweeps. This demonstrates that the observed χ' peak in LaRh₂As₂ is unlikely associated with the nature of type-I superconductivity.

Instead, the reversible character of the χ' peak suggests the transition between an irreversible and a reversible superconducting vortex state in a type-II superconductor [32]. In the irreversible state, expelling external fields leads to a negative χ' signal. In the reversible state in higher fields, the magnetization decreases in magnitude with increasing fields and the positive magnetization slope ($dM/dH > 0$) results in the positive χ' . The positive χ' approaches nearly zero as the normal state is realized in further fields. This is also consistent with the absence of the peak at zero field [see the inset of Fig. 3(b)] and the decreasing size on approaching T_c [the 250 mK data in the inset of Fig. 4(a)] as the reversible region gradually shrinks and vanishes when approaching T_c at zero field. Within the picture of type-II superconductivity, we define the upper critical-field H_{c2} at the peak. Additionally,

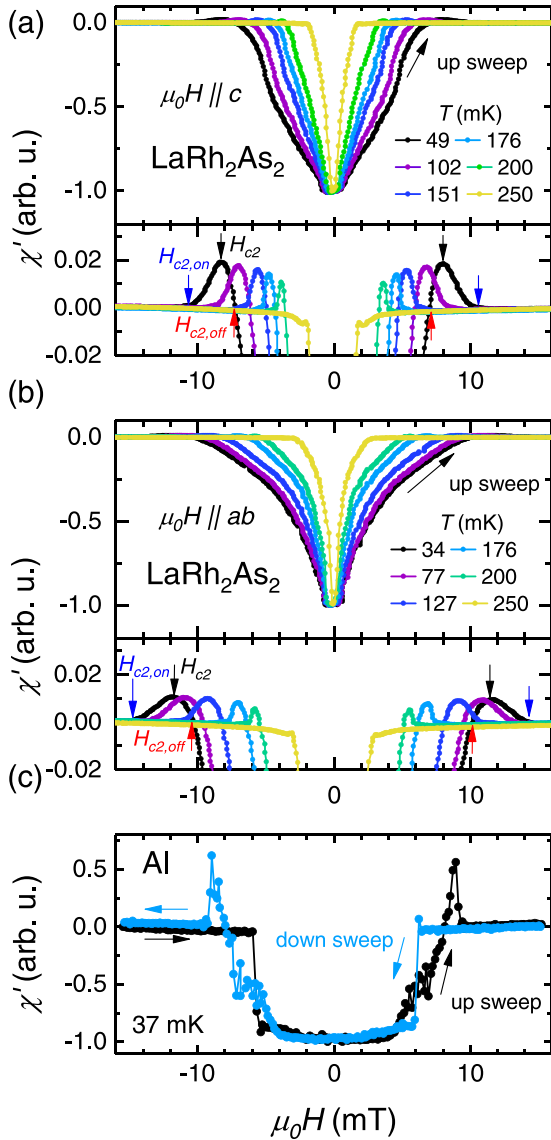


FIG. 4. Field dependence of $\chi'(H)$ for LaRh_2As_2 with $H \parallel c$ (a) and $H \parallel ab$ (b) at different temperatures. The data are obtained on a field sweep from -16 mT to $+16$ mT. The lower panels emphasize the χ' peak. H_{c2} is defined at the peak position. $H_{c2,on}$ ($H_{c2,off}$) denotes the onset of the peak on the high(low)-field side. (c) $\chi'(H)$ of an aluminum sample measured at 37 mK for up and down sweeps. Aluminum exhibits the typical asymmetric differential paramagnetic effect for a type-I superconductor.

we define the onset $H_{c2,on}$ and offset $H_{c2,off}$ fields as given in Figs. 4(a) and 4(b) in between which the reversible state develops.

The superconducting H_{c2} phase diagram for $H \parallel c$ and $H \parallel ab$ is shown in Fig. 5. The temperature dependence of H_{c2} is well described by the Werthamer-Helfand-Hohenberg (WHH) model without including the Pauli limiting effect [33] given by

$$\ln\left(\frac{1}{t}\right) = \psi\left(\frac{1}{2} + \frac{\bar{h}}{2t}\right) - \psi\left(\frac{1}{2}\right), \quad (2)$$

where ψ is the digamma function, $t = T/T_c$ and $\bar{h} = 4H_{c2}/\pi^2(-dH/dt)_{t=1}$, with $T_c = 0.296$ K defined at the onset

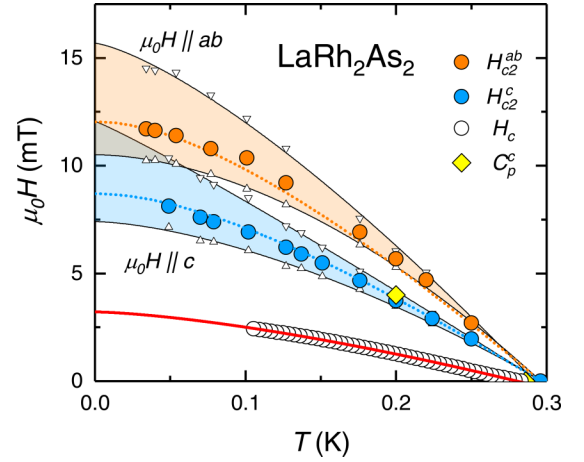


FIG. 5. Superconducting phase diagram of LaRh_2As_2 for $H \parallel c$ and $H \parallel ab$. The H_{c2} as well as the onset (downward triangles) and offset (upward triangles) of the superconducting transition are determined from the χ' measurements [the bottom panels of the Figs. 4(a) and 4(b)]. The H_{c2} determined from the specific-heat measurements (yellow diamond) is also shown [Fig. 3(c)]. The dotted lines are fits using the dirty-limit WHH model. The black solid lines are guides to the eye. The thermodynamic critical field H_c deduced from the superconducting C/T data is denoted by open circles and extrapolated to $T = 0$ using $H_c = H_c(0)[1 - (T/T_c)^n]$ (red line).

of the transition in $\chi'(T)$ [see Fig. 3(b)]. Using Eq. (2) with $dH/dT|_{T_c} = -59$ mT/K and $dH/dT|_{T_c} = -42$ mT/K, we obtain that the zero-temperature limit of $H_{c2}(0)$ is 12 and 8.6 mT for $H \parallel ab$ and $H \parallel c$, respectively. The small anisotropy of H_{c2} observed here indicates that the Fermi surface of LaRh_2As_2 is rather three dimensional.

The good agreement of the H_{c2} curves with the WHH model implies that superconductivity in LaRh_2As_2 is orbitally limited with a critical field that lies well below the expected BCS Pauli limit of $H_p \approx 1.84T_c \approx 0.5$ T. Therefore a possible anisotropic enhancement of the Pauli limiting field due to, e.g., the Rashba effect, remains invisible in the superconducting phase diagram. Accordingly, the phase transition between even and odd parity, as observed in CeRh_2As_2 [1], is only possible when the Pauli limit is smaller than the orbital limit, which is not the case here.

E. Type-II superconductivity

We estimate the thermodynamic critical field (H_c) in order to extract further superconducting parameters. H_c is determined from the free-energy difference between the normal and the superconducting states, $\Delta F = F_n - F_s$, obtained from the C/T data by integration of the entropy difference [34–37],

$$\Delta F(T) = \frac{\mu_0 H_c^2(T)}{2} = \int_{T_c}^T \int_{T_c}^{T'} \frac{C_s - C_n}{T''} dT'' dT'. \quad (3)$$

Here C_n and C_s are given by the specific heat for 10 mT and zero field, respectively [Fig. 3(c)]. The specific-heat data were integrated from T_c down to 0.1 K where the experimental data are available. As shown in Fig. 5, the resulting H_c is smaller than the measured H_{c2} with the extrapolated $H_c(0)$ of 3.2 mT.

By using the values of H_c and H_{c2} , we calculate the Ginzburg-Landau parameters, $\kappa_{GL}^{ab} = H_{c2\parallel c}(0)/\sqrt{2}H_c(0) = 1.9$ and $\kappa_{GL}^c = H_{c2\parallel ab}(0)/\sqrt{2}H_c(0) = 2.7$. The $\kappa_{GL} > 1/\sqrt{2}$ indicates type-II superconductivity. The lower critical field, $H_{c1} = (H_c/\sqrt{2}\kappa_{GL}^{ab}) \ln(\kappa_{GL}^{ab})$, is estimated to 0.8 mT. This H_{c1} seems to agree with the field where χ' starts to deviate from the plateau-like minimum [see Fig. 4(a)]. The coherence lengths $\xi_{GL}^{ab} = 200$ nm and $\xi_{GL}^c = 140$ nm were estimated using $\xi_{GL}^{ab} = [\Phi_0/2\pi\mu_0 H_{c2\parallel c}(0)]^{1/2}$ and $\xi_{GL}^c = \Phi_0/2\pi\xi_{GL}^{ab}(0)H_{c2\parallel ab}(0)$. The penetration depths are given by the relations of $\lambda_{ab} = \kappa_{GL}^{ab}\xi_{GL}^{ab} = 370$ nm and $\lambda_c = (\kappa_{GL}^c)^2\xi_{GL}^c\xi_{GL}^{ab}/\lambda_{ab} = 520$ nm.

In order to classify the superconductivity in terms of dirty or clean limit, we estimated the mean-free path with [38,39]:

$$l = 1.27 \times 10^4 \cdot [\rho_0(n^{2/3}S/S_F)]^{-1} \approx \frac{1200 \mu\Omega \text{cm}\text{\AA}^{-1}}{k_F^2 \rho_0}. \quad (4)$$

With $k_F = 0.57 \text{\AA}^{-1}$ from the DFT calculations, assuming a spherical Fermi surface ($S/S_F = 1$) and using the experimental value of $\rho_0 = 10 \mu\Omega \text{cm}$, the mean-free path is about $l = 36$ nm. The ratio $l/\xi_{GL}^{ab} \approx 0.18$ suggests that the superconductivity in LaRh₂As₂ is in the dirty limit. The fact that the H_{c2} in LaRh₂As₂ is very small naturally leads to a large Ginzburg-Landau coherence length; hence the clean limit for this material is only possible for very high-purity crystals with residual resistivity at least 15 times smaller than the sample we measured. Even if we consider an uncertainty of one order of magnitude in the estimation of the mean-free path, the superconductivity is still within the dirty limit. In comparison, the weak-coupling noncentrosymmetric superconductor LaPt₃Si has comparable values of the residual resistivity (2 times larger) [36] but a higher H_{c2} (40 times larger), and it was also estimated to be in the dirty limit. Hence, we can safely suggest that the superconductivity in LaRh₂As₂ is in the dirty limit.

F. Estimation of electron-phonon coupling constant

We estimate the strength of the electron-phonon ($e-ph$) interactions for $T_c = 0.28$ K based on the Eliashberg theory. A measure for the strength of the $e-ph$ interaction, parameterized by λ_{e-ph} , is the mass enhancement of the quasiparticles in the normal state. According to the microscopic Eliashberg theory, the coupling constant depends on the $e-ph$ spectral function $\alpha^2F(\omega)$ and the weak Coulomb pseudopotential μ^* . As $\alpha^2F(\omega)$ is unknown, we adopt several typical models $\alpha^2F_{\text{model}}(\omega)$ for the $e-ph$ coupling functions and estimate the range of λ_{e-ph} required to reproduce T_c for the different distributions of the spectral weights. We choose the maximal phonon frequency of $\hbar\omega_{\text{max}} = 36$ meV in agreement with the maximal phonon frequency estimated from DFT calculations. The variation with frequency of $\alpha^2F_{\text{model}}(\omega)$ is compared by considering the averaged frequencies

$$\langle\omega\rangle_1 = \frac{\int_0^\infty d\omega \omega \alpha^2 F_{\text{model}}(\omega)}{\int_0^\infty d\omega \frac{\alpha^2 F_{\text{model}}(\omega)}{\omega}}; \langle\omega\rangle_2 = \frac{\int_0^\infty d\omega \omega \alpha^2 F_{\text{model}}(\omega)}{\int_0^\infty d\omega \alpha^2 F_{\text{model}}(\omega)}. \quad (5)$$

The model $e-ph$ coupling function is scaled by a constant prefactor so as to reproduce the observed T_c . T_c is calculated by solving the linearized Eliashberg equations for this scaled

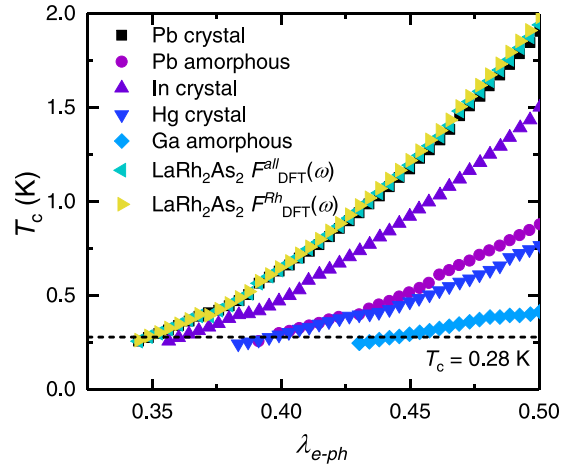


FIG. 6. T_c as a function of λ_{e-ph} for various model spectra. The λ_{e-ph} values reproducing $T_c = 0.28$ K marked by the horizontal dotted line are listed in Table I.

function assuming a standard value for the Coulomb pseudopotential $\mu^* \sim 0.13$. From the scaled $\alpha^2F(\omega)$, we deduce the corresponding electron-phonon mass enhancement as

$$\lambda_{e-ph} = 2 \int_0^\infty \frac{d\omega}{\omega} \alpha^2 F(\omega). \quad (6)$$

The variation of T_c with λ_{e-ph} for each model spectrum is shown in Fig. 6; λ_{e-ph} and averaged frequencies of $\langle\omega\rangle_1$ and $\langle\omega\rangle_2$ corresponding to the experimental $T_c = 0.28$ K are listed in Table I. While the estimated λ_{e-ph} has a variation depending on the models, they are in the range of $\lambda_{e-ph} \sim 0.34-0.44$, consistently pointing to LaRh₂As₂ being in the weak-coupling regime.

G. Electronic structure calculations

To get more insight into the electronic structure and the states relevant for the superconductivity, we carried out density-functional calculations. Since there was no precise information about the internal coordinates of the atoms, we relaxed their position with respect to the total energy using the experimental lattice parameters. As starting values, we used the closely related LaIr₂As₂ structure [27]. The obtained free parameters for the different Wyckoff positions are La

TABLE I. Averaged frequencies calculated for the model spectra and the mass enhancement required to reproduce $T_c = 0.28$ K. Although the λ_{e-ph} have a certain spread they all point to the weak-coupling regime.

	$\hbar\langle\omega\rangle_1$ [K]	$\hbar\langle\omega\rangle_2$ [K]	λ_{e-ph}
Pb crystal	181	206	0.34
Pb amorphous	130	194	0.39
Hg crystal	90	150	0.39
In crystal	158	201	0.36
Ga amorphous	82	168	0.44
$F_{\text{DFT}}^{\text{all}}(\omega)$	191	223	0.34
$F_{\text{DFT}}^{\text{Rh}}(\omega)$	184	212	0.34

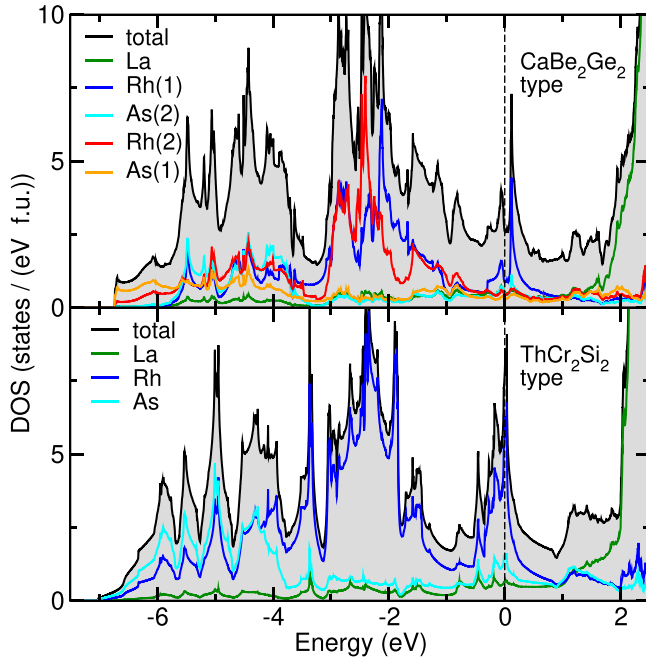


FIG. 7. Total and partial electronic DOS of LaRh_2As_2 for the experimentally observed CaBe_2Ge_2 -type structure (upper panel) and the fictitious ThCr_2Si_2 -type structure (lower panel). The Fermi level is at zero energy.

$2c z = 0.7544$, $\text{Rh}(2) 2c z = 0.1195$ and $\text{As}(2) 2c z = 0.3641$. The calculated equilibrium positions vary only slightly with respect to LaIr_2As_2 [$\text{La} 2c z = 0.7550$, $\text{Ir}(2) 2c z = 0.1161$ and $\text{As}(2) 2c z = 0.3625$], providing additional trust in the accuracy of the DFT calculations. The energy gain from the relaxation is about 1 meV per atom only. The corresponding differences for the valance band states are insignificant.

The resulting total and partial densities of states (DOS) for the CaBe_2Ge_2 -type structure (with La on the Ca site without inversion symmetry) and relaxed Wyckoff positions are shown in Fig. 7 (upper panel). The upper part of the valence band (between about -3 and -1 eV) is dominated by Rh states. Arsenic states contribute mostly to the bonding region of the valence band (between about -3.5 and -6.5 eV).

The difference between the two crystallographically different Rh-As layers is rather pronounced. The states of the Rh(1)-centered layer are significantly higher in energy than those of the As(1)-centered layer, in particular at the band bottom. This is a consequence of the shorter and thus stronger Rh(2)-As(1) bonds (see subsection “Crystal structure”), which in turn leads to more hybridized orbitals. At the Fermi level E_F , all atoms contribute almost equally apart from Rh(1) which exhibits a pronounced double peak feature near E_F . The Fermi level falls in the dip between the two peaks.

Since many of the rare-earth transition metal pnictides with a 1:2:2 stoichiometry crystallize in the ThCr_2Si_2 -type structure (with the rare-earth atom on the inversion site), we calculated for comparison LaRh_2As_2 in this fictitious structure, containing only Rh-centered Rh-As layers. We used the lattice parameters for the experimentally observed CaBe_2Ge_2 -type structure, relaxing the $4e$ Wyckoff position of As ($z = 0.3751$). The resulting DOS are shown in Fig. 7

(lower panel). The DOS for the fictitious compound is similar to the real compound (upper panel), with dominating Rh states between about -3 and -1 eV. Since the fictitious compound contains only Rh-centered Rh-As layers, the peak around the Fermi level is even more pronounced. The high value of the DOS at E_F is likely the reason why the compound does not crystallize in the ThCr_2Si_2 -type structure. Comparing the calculated total energies for both structures, the observed CaBe_2Ge_2 -type structure is favored by 1.12 eV per formula unit. For the closely related LaNi_2As_2 compound for which both polymorphs exist [28], the calculated energy difference between them amounts to only 300 meV, taking into account that the experimental c/a ratio reduces the difference further to 150 meV. We conclude that the large energy difference of 1.12 eV for the two polymorphs for LaRh_2As_2 makes it unlikely that the ThCr_2Si_2 -type structure is stable for this compound at ambient conditions. One has to keep in mind though that these calculations are valid for $T = 0$ and other additional factors come into play at the high temperature of crystallization.

The calculated DOS at E_F yields a bare Sommerfeld coefficient γ_0 between 6.1 and 7.5 mJ/mol K^2 , depending on the choice of the exchange-correlation functional (LDA vs GGA) or the structural input (Wyckoff positions of LaIr_2As_2 vs relaxed positions). Taking into account the experimental $\gamma = 9.4$ mJ/mol K^2 , we can estimate a mass renormalization $\lambda = \gamma/\gamma_0 - 1 = 0.4 \pm 0.14$. This compares rather well with the electron-phonon coupling-constant $\lambda_{e-ph} \sim 0.34-0.44$ calculated from α^2F .

The band structure of LaRh_2As_2 is shown in Fig. 8. Comparing the overall in-plane dispersion (Γ -X-M- Γ) with the out-of-plane-dispersion (Γ -Z), a rather pronounced two dimensionality of the compound is observed. In addition, the influence of SOC is rather small. Typical band splittings by SOC at the Γ point are of the order of 100 to 150 meV (see Fig. 8).

H. Comparison to other (locally) noncentrosymmetric superconductors

We also calculated the band structure of the isostructural CeRh_2As_2 compound to check whether the small differences and details in the crystal structure have a significant influence on the states near the Fermi level. This could be well possible because of the strongly pronounced Rh(1) peak near E_F . To separate the influence of the Ce- $4f$ electrons from that of the crystal structure, we treated the $4f$ electrons as localized, nonhybridizing core states. The resulting band structure and DOS are very similar to that of LaRh_2As_2 ; the Rh(1)-related peak remains above E_F . This strongly suggests that the unconventional superconductivity in the Ce system is intimately related to the hybridization of the $4f$ states with the valence electrons.

For both (La and Ce) compounds, SOC originates mainly from the Rh. However, Ce- $4f$ electrons—as in heavy-fermion systems in general—have very flat bands coming from the hybridization of the f electrons with the conduction electrons (here mainly the Rh d electrons). Compared with the bandwidth of these flat bands, SOC is then large and has a strong effect on the electronic properties of the system.

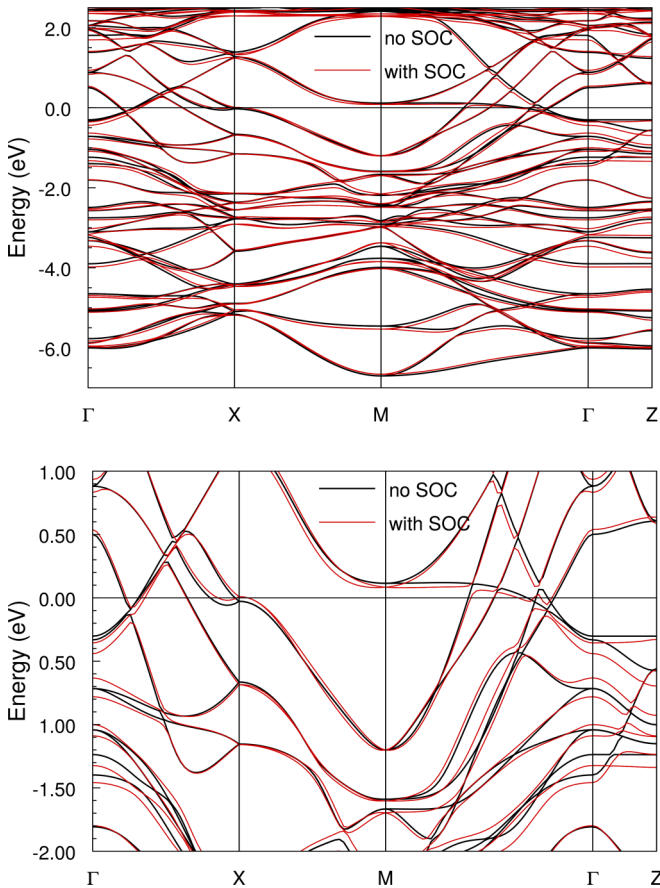


FIG. 8. Band structure of LaRh_2As_2 for the experimentally observed CaBe_2Ge_2 -type structure with and without SOC, full valence band (upper panel), and zoom-in to the Fermi level at zero energy (lower panel).

This is in line with the observation that in noncentrosymmetric heavy-fermion superconductors, where the Ce position has the same local symmetry C_{4v} as in CeRh_2As_2 , unconventional superconductivity occurs, whereas the La sister compounds do not show any unconventional features of the superconducting state. For example, CeRhSi_3 presents a huge anisotropy of the critical field under pressure where the $T_c = 1.5$ K is maximum, similar to CeRh_2As_2 . In contrast, LaRhSi_3 has a roughly isotropic superconducting state with a T_c of 0.9 K and low critical-field values [15]. In penetration depth experiments, it was also found that CePt_3Si has an unconventional gap structure with line nodes, but LaPt_3Si has a conventional full gap [14].

Let us discuss the similarity of T_c in CeRh_2As_2 and LaRh_2As_2 . As presented above, all the experimental evidence and calculations (Eliashberg theory) suggest that LaRh_2As_2 is an electron-phonon-mediated superconductor in the weak-coupling limit. No additional phase occurs that might influence the superconducting state. In contrast, CeRh_2As_2 has all the characteristics of unconventional superconductivity as in other heavy-fermion systems, where a spin (or valence)-fluctuation mechanism was proposed [40]. First, the effective mass is extremely high, pointing at a large DOS. This should change the T_c significantly, even if all other parameters like the coupling constant and characteristic phonon

energy were the same in both systems. Second, in CeRh_2As_2 an additional phase exists at 0.4 K that was suggested to be a quadrupole density wave order with a complex phase diagram [41] and an antiferromagnetic phase was observed below 0.25 K [18]. For both, the influence on the superconducting state is not settled yet. Third, CeRh_2As_2 shows signs of quantum criticality [1] and antiferromagnetic fluctuations in the normal state [42]. It hence seems likely that a different coupling mechanism is at play here, where the coupling constant as well as characteristic energies are different so that the matching T_c is a coincidence.

LaRh_2As_2 and CeRh_2As_2 are not the only superconducting materials with the CaBe_2Ge_2 -type structure. For example, LaPt_2Si_2 and SrPt_2As_2 become superconducting at 1.77 and 5.2 K, respectively. Moreover, those materials have a charge-density wave (CDW) transition at 122 and 470 K, respectively [43,44]. Interestingly, they show a small enhancement of H_{c2} over the expectation value of the WHH theory. This behavior was attributed to a possible interplay between superconductivity and CDW. By contrast, other compounds, like LaPd_2Bi_2 [45], LaPd_2Sb_2 [46] and the low-temperature phase of SrPd_2Sb_2 [47], only exhibit superconductivity with properties within the conventional frame of electron-phonon-mediated superconductivity.

Another comparable La system with a crystalline structure that breaks inversion symmetry (CeNiC_2 -type orthorhombic structure with space group $\text{Amm}2$) is LaNiC_2 [48]. Time-reversal symmetry was reported to be broken in the superconducting state in this compound [49]. Also, LaNiC_2 was suggested to possess an unconventional superconducting gap structure (nodal gap and multigap) [50,51], and superconductivity develops in the vicinity of a magnetic quantum critical point [52].

The conventional superconducting properties of LaRh_2As_2 as well as other materials, which lack inversion symmetry locally or globally but show no additional ordered state, suggest that breaking the inversion symmetry as the only key ingredient is not sufficient to obtain unconventional properties. Rather, it seems that the lack of inversion symmetry has to be combined with superconductivity that appears near other quantum phases such as magnetism, CDW, and multipolar phases in the proximity to quantum critical points in order to induce unconventional superconductivity and strong effects of antisymmetric SOC [53].

IV. CONCLUSION AND SUMMARY

The combination of SOC and the absence of inversion symmetry in a compound can result in unusual properties. We therefore investigated the compound LaRh_2As_2 which crystallizes in the tetragonal CaBe_2Ge_2 -type structure where inversion symmetry is present at the global level but absent in the La layers. Resistivity, specific heat, and ac-susceptibility measurements prove bulk superconductivity below a bulk $T_c = 0.28$ K. The H - T superconducting phase diagrams show orbitally limited H_{c2} behavior for fields both parallel and perpendicular to the tetragonal c axis, with a rather weak anisotropy. The H_{c2} are up to a factor of about 3 above the thermodynamic critical field, pointing to type-II superconductivity.

Both an analysis based on the Eliashberg theory and a comparison between the theoretically calculated and the experimentally determined Sommerfeld coefficient indicate the electron-phonon coupling constant to be of the order of 0.4, implying weak-coupling superconductivity. The density-functional calculations further reveal that the electronic DOS at the Fermi level is predominantly due to the Rh(1) atoms from the Rh-centered Rh-As layer. The much lower energy level of Rh(2) atoms results in the CaBe₂Ge₂-type structure being energetically favored in comparison with the ThCr₂Si₂-type structure.

Despite having the same crystal structure and similar ASOC as the Ce analog, LaRh₂As₂ appears as a conventional superconductor. The critical fields are entirely given by the orbital limit which is well below the expected Pauli limiting field. It remains an open question whether a higher orbital limit from large effective masses would be sufficient to give rise to a similar two-phase superconductivity driven by Pauli physics, as in CeRh₂As₂, or whether additional degrees of

freedom and/or additional interactions connected with the 4*f* electrons are needed. In real materials like CeRh₂As₂ both effects are related since the proximity to ordered *f*-electron states is at the origin of the large effective masses. We can conclude that symmetry is not the only required ingredient for the observation of unconventional behavior related with ASOC.

ACKNOWLEDGMENTS

U. Nitzsche is acknowledged for technical support. E.H., C.G. and G.Z. acknowledge funding from the joint Agence National de la Recherche (ANR) and DFG program FermiNESt (Project No. 316740996) through Grants No. GE602/4-1 (C.G.) and ZW77/5-1 (G.Z.). J.F.L., S.Z., and E.H. received financial support from the Max Planck Research Group “Physics of Unconventional Metals and Superconductors” by the Max Planck Society.

-
- [1] S. Khim, J. F. Landaeta, J. Banda, N. Bannor, M. Brando, P. M. R. Brydon, D. Hafner, R. K uchler, R. Cardoso-Gil, U. Stockert, A. P. Mackenzie, D. F. Agterberg, C. Geibel, and E. Hassinger, *Science* **373**, 1012 (2021).
- [2] F. Steglich, J. Aarts, C. D. Bredl, W. Lieke, D. Meschede, W. Franz, and H. Sch afer, *Phys. Rev. Lett.* **43**, 1892 (1979).
- [3] T. T. M. Palstra, A. A. Menovsky, J. van den Berg, A. J. Dirkmaat, P. H. Kes, G. J. Nieuwenhuys, and J. A. Mydosh, *Phys. Rev. Lett.* **55**, 2727 (1985).
- [4] M. Rotter, M. Tegel, and D. Johrendt, *Phys. Rev. Lett.* **101**, 107006 (2008).
- [5] E. Bauer and M. Sigrist, *Non-Centrosymmetric Superconductors: Introduction and Overview*, Lecture Notes in Physics, Vol. 847 (Springer-Verlag, Berlin Heidelberg, 2012).
- [6] M. Smidman, M. B. Salamon, H. Q. Yuan, and D. F. Agterberg, *Rep. Prog. Phys.* **80**, 036501 (2017).
- [7] T. Yoshida, M. Sigrist, and Y. Yanase, *Phys. Rev. B* **86**, 134514 (2012).
- [8] D. Maruyama, M. Sigrist, and Y. Yanase, *J. Phys. Soc. Jap.* **81**, 034702 (2012).
- [9] M. Sigrist, D. F. Agterberg, M. H. Fischer, J. Goryo, F. Loder, S.-H. Rhim, D. Maruyama, Y. Yanase, T. Yoshida, and S. J. Youn, *J. Phys. Soc. Jap.* **83**, 061014 (2014).
- [10] X. Zhang, Q. Liu, J.-W. Luo, A. J. Freeman, and A. Zunger, *Nat. Phys.* **10**, 387 (2014).
- [11] Z. Wang, J. Berlinsky, G. Zwirnagl, and C. Kallin, *Phys. Rev. B* **96**, 174511 (2017).
- [12] K. Nogaki, A. Daido, J. Ishizuka, and Y. Yanase, *Phys. Rev. Research* **3**, L032071 (2021).
- [13] R. Madar, P. Chadouet, J. P. Senateur, S. Zemni, and D. Tranqui, *J. Less-Common Met.* **133**, 303 (1987).
- [14] R. L. Ribeiro, I. Bonalde, Y. Haga, R. Settai, and Y. Ōnuki, *J. Phys. Soc. Jpn.* **78**, 115002 (2009).
- [15] R. Settai, Y. Miyauchi, T. Takeuchi, F. L evy, I. Sheikin, and Y. Ōnuki, *J. Phys. Soc. Jpn.* **77**, 073705 (2008).
- [16] S. Palazzese, J. F. Landaeta, D. Subero, E. Bauer, and I. Bonalde, *J. Phys.: Condens. Matter* **30**, 255603 (2018).
- [17] H. Wilhelm, T. L uhmann, T. Rus, and F. Steglich, *Rev. Sci. Instrum.* **75**, 2700 (2004).
- [18] M. Kibune, S. Kitagawa, K. Kinjo, S. Ogata, M. Manago, T. Taniguchi, K. Ishida, M. Brando, E. Hassinger, H. Rosner, C. Geibel, and S. Khim, *Phys. Rev. Lett.* **128**, 057002 (2022).
- [19] T. Hagino, Y. Seki, S. Takayanagi, N. Wada, and S. Nagata, *Phys. Rev. B* **49**, 6822 (1994).
- [20] R. G. Parr, in *Horizons of Quantum Chemistry*, edited by K. Fukui and B. Pullman (Springer, Dordrecht, 1980), pp. 5–15.
- [21] W. Kohn and L. J. Sham, *Phys. Rev.* **140**, A1133 (1965).
- [22] G. Kresse and J. Furthm uller, *Comput. Mater. Sci.* **6**, 15 (1996).
- [23] K. Koepnik and H. Eschrig, *Phys. Rev. B* **59**, 1743 (1999).
- [24] J. P. Perdew and Y. Wang, *Phys. Rev. B* **45**, 13244 (1992).
- [25] J. P. Perdew, K. Burke, and M. Ernzerhof, *Phys. Rev. Lett.* **77**, 3865 (1996).
- [26] A. Togo and I. Tanaka, *Scr. Mater.* **108**, 1 (2015).
- [27] U. Pfannenschmidt, F. Behrends, H. Lincke, M. Eul, K. Schaefer, H. Eckert, and R. Poettgen, *Dalton Transactions* **41**, 14188 (2012).
- [28] E. El Ghadraoui, J. Pivan, R. Gu erin, O. Pena, J. Padiou, and M. Sergent, *Mater. Res. Bull.* **23**, 1345 (1988).
- [29] R. A. Hein and R. L. Falge, *Phys. Rev.* **123**, 407 (1961).
- [30] S. Yonezawa and Y. Maeno, *Phys. Rev. B* **72**, 180504(R) (2005).
- [31] L. L. Zhao, S. Lausberg, H. Kim, M. A. Tanatar, M. Brando, R. Prozorov, and E. Morosan, *Phys. Rev. B* **85**, 214526 (2012).
- [32] S. Banerjee, S. Saha, N. Patil, S. Ramakrishnan, A. Grover, S. Bhattacharya, G. Ravikumar, P. Mishra, T. Rao, V. Sahni, C. Tomy, G. Balakrishnan, D. Mck. Paul, and M. Higgins, *Physica C: Superconductivity* **308**, 25 (1998).
- [33] E. Helfand and N. R. Werthamer, *Phys. Rev.* **147**, 288 (1966).
- [34] E. Bauer, G. Hilscher, H. Michor, C. Paul, E. W. Scheidt, A. Griбанov, Y. Seropegin, H. No el, M. Sigrist, and P. Rogl, *Phys. Rev. Lett.* **92**, 027003 (2004).

- [35] E. Bauer, A. Grytsiv, X.-Q. Chen, N. Melnychenko-Koblyuk, G. Hilscher, H. Kaldarar, H. Michor, E. Royanian, G. Giester, M. Rotter, R. Podloucky, and P. Rogl, *Phys. Rev. Lett.* **99**, 217001 (2007).
- [36] F. Kneidinger, H. Michor, A. Sidorenko, E. Bauer, I. Zeiringer, P. Rogl, C. Blaas-Schenner, D. Reith, and R. Podloucky, *Phys. Rev. B* **88**, 104508 (2013).
- [37] Y. Kawamura, S. Deminami, L. Salamakha, A. Sidorenko, P. Heinrich, H. Michor, E. Bauer, and C. Sekine, *Phys. Rev. B* **98**, 024513 (2018).
- [38] T. P. Orlando, E. J. McNiff, S. Foner, and M. R. Beasley, *Phys. Rev. B* **19**, 4545 (1979).
- [39] S. Ramakrishnan, K. Ghosh, A. D. Chinchure, V. R. Marathe, and G. Chandra, *Phys. Rev. B* **52**, 6784 (1995).
- [40] N. Mathur, F. M. Grosche, S. R. Julian, I. R. Walker, D. M. Freye, R. K. W. Haselwimmer, and G. G. Lonzarich, *Nature* **394**, 39 (1998).
- [41] D. Hafner, P. Khanenko, E.-O. Eljaouhari, R. K uchler, J. Banda, N. Bannor, T. L uhmann, J. F. Landaeta, S. Mishra, I. Sheikin, E. Hassinger, S. Khim, C. Geibel, G. Zwicknagl, and M. Brando, *Phys. Rev. X* **12**, 011023 (2022).
- [42] S. Kitagawa, M. Kibune, K. Kinjo, M. Manago, T. Taniguchi, K. Ishida, M. Brando, E. Hassinger, C. Geibel, and S. Khim, *J. Phys. Soc. Jap.* **91**, 043702 (2022).
- [43] R. Gupta, S. K. Dhar, A. Thamizhavel, K. P. Rajeev, and Z. Hossain, *J. Phys.: Condens. Matter* **29**, 255601 (2017).
- [44] K. Kudo, Y. Nishikubo, and M. Nohara, *J. Phys. Soc. Jpn.* **79**, 123710 (2010).
- [45] S. Ganesanpotti, T. Yajima, T. Tohyama, Z. Li, K. Nakano, Y. Nozaki, C. Tassel, Y. Kobayashi, and H. Kageyama, *J. Alloys Compd.* **583**, 151 (2014).
- [46] Q. Mu, B. Pan, B. Ruan, T. Liu, K. Zhan, L. Shan, G. Chen, and Z. Ren, *Sci. China Phys. Mech. Astron.* **61**, 127409 (2018).
- [47] N. Kase, H. Suzuki, T. Tsukamoto, T. Nakano, and N. Takeda, *J. Phys. Soc. Jpn.* **85**, 043701 (2016).
- [48] W. Lee, H. Zeng, Y. Yao, and Y. Chen, *Physica C: Superconductivity* **266**, 138 (1996).
- [49] A. D. Hillier, J. Quintanilla, and R. Cywinski, *Phys. Rev. Lett.* **102**, 117007 (2009).
- [50] I. Bonalde, R. L. Ribeiro, K. J. Syu, H. H. Sung, and W. H. Lee, *New J. Phys.* **13**, 123022 (2011).
- [51] J. Chen, L. Jiao, J. L. Zhang, Y. Chen, L. Yang, M. Nicklas, F. Steglich, and H. Q. Yuan, *New J. Phys.* **15**, 053005 (2013).
- [52] J. F. Landaeta, D. Subero, P. Machado, F. Honda, and I. Bonalde, *Phys. Rev. B* **96**, 174515 (2017).
- [53] J. F. Landaeta, D. Subero, D. Catal a, S. V. Taylor, N. Kimura, R. Settai, Y. Onuki, M. Sigrist, and I. Bonalde, *Phys. Rev. B* **97**, 104513 (2018).